

1 The contribution of the ankyrin repeat 2 domain of TRPV1 as a thermal module

3

4 E. Ladrón-de-Guevara

5 G. E. Rangel-Yescas

6 D. A. Fernández-Velasco

7 A. Torres-Larios

8 T. Rosenbaum

9 L. D. Islas

10

11 Abstract

12 The TRPV1 cation non-selective ion channel plays an essential role in thermosensation and perception of
13 other noxious stimuli. TRPV1 can be activated by low pH, high temperature or naturally occurring
14 pungent molecules such as allicin, capsaicin or resiniferatoxin. Its noxious thermal sensitivity makes it an
15 important participant as a thermal sensor in mammals. However, details of the mechanism of channel
16 activation by increases in temperature remain unclear. Here we used a combination of approaches to try
17 to understand the role of the ankyrin repeat domain (ARD) in channel behavior. First, a computational
18 modeling approach by coarse-grained molecular dynamics simulation of the whole TRPV1 embedded in
19 a phosphatidylcholine (POPC) and phosphatidylethanolamine (POPE) membrane provides insight into
20 the dynamics of this channel domain. Global analysis of the structural ensemble shows that the ankyrin
21 repeat domain is a region that sustains high fluctuations during dynamics at different temperatures. We
22 then performed biochemical and thermal stability studies of the purified ARD by means of circular
23 dichroism and tryptophan fluorescence and demonstrate that this region undergoes structural changes
24 at similar temperatures that lead to TRPV1 activation. Our data suggest that the ARD is a dynamic
25 module and that it may participate in controlling the temperature sensitivity of TRPV1.

26 Statement of Significance

27 This work demonstrates that the temperature-dependent dynamics of the ankyrin repeat domain (ARD)
28 of TRPV1 channels, as probed by coarse-grained molecular dynamics, corresponds to the experimentally
29 determined dynamics of an isolated ARD domain. These results show that this region of TRPV1 channels
30 undergoes significant conformational change as a function of increased temperature and suggest that it
31 participates in the temperature-dependent structural changes that lead to channel opening.

32 Keywords:

33 Plasma membrane, trpv1, molecular dynamics, coarse-grained, temperature, circular dichroism,
34 tryptophan fluorescence, thermal shift.

35 Introduction

36 TRPV1 is a non-specific cation channel implicated in nociception by chemicals, temperature, and pH (1–
37 3). This channel is one of the chemosensors involved in the sensation of pain and thermal stimuli and it
38 participates in a diverse range of cellular processes (2, 4). The latter has been evidenced from studies
39 where deletion of TRPV1 in mice alters noxious and mild temperature sensation (5, 6), while knock-out
40 of other thermoTRPs such as TRPV2, TRPV3, and TRPV4 shows little effects in sensory transduction in
41 rodents (6–8). Moreover, while deletion of TRPV1 in rodents does not affect corporal temperature,
42 blockage of TRPV1 *in vivo* triggers hyperthermia (9).

43 The rat TRPV1 structure is a tetramer (Fig. 1a), with every monomer consisting of 838 amino acids (Fig.
44 1c). The structure solved by cryo-EM is from a minimal-functional TRPV1 that lacks 100 amino acids from
45 the N-termini and 80 amino acids in the C-termini and which is also missing a longer S5-pore
46 extracellular loop named the turret. This minimal-functional 586 amino acid construct provides a model
47 for the full-length channel, although without unfolded loops. In TRPV1, the structure of the membrane-
48 embedded domains is canonical with other ion channels like voltage-gated potassium, sodium and
49 calcium ion channels. A tetramer is formed by a voltage sensing domain (VSD)-like domain, surrounding
50 a pore formed by the contribution of the four pore domains (PD) of each subunit.

51 The C-terminus of TRPV1 has been shown to be functionally important. Several modulating lipids, such
52 as PIP2 and LPA bind in this region (10, 11). In the cryo-EM structures, the alpha helix after the S6
53 transmembrane segment is well defined and is known as the TRP-box; it is a conserved domain in almost
54 all the members of the TRP family. In all the solved structures for TRPV1 (12–14), TRPV 2 (15), TRPV3

55 (16), TRPV4 (17), TRPV5 (18) and TRPV6 (19), the TRP-box is folded in the same manner. In the case of
56 TRPV1, Cryo-EM experiments show that the TRP-box displays a conformational change when the
57 channel is bound to capsaicin (13), or resiniferatoxin and double-knot toxin (DkTx) together (13), similar
58 to what happens in TRPV2 sensitized by 2-Aminoethoxydiphenyl Borate (2-APB) (15). Until now the
59 structure of the distal part of the C-terminus remains unknown, but there is some evidence that it is
60 located near the ankyrin repeat domain (ARD), and that these two structures may undergo intradomain
61 interactions (20).

62 The ARD and the membrane proximal domain (MPD), a structure located between the ARD and the first
63 transmembrane segment, have a non-canonical interaction only seen in TRP channels. A “finger” loop
64 from ANK4 touches the MPD at a recognition site in a neighboring subunit (Figure 1a and Sup. Fig. 1)
65 (12, 19). Although some of the functions of these domains are still not known, others have been well
66 characterized and include the direct interaction of the ARD with calmodulin (18, 21) and the possible
67 participation of the MPD in heat activation (22). Thus, the ARD and MPD are functional regulatory
68 domains and it should be noted that, before the first cryo-EM structures for TRP channels were
69 obtained, the intracellular domains were visualized as individual and not interconnected domains.
70 Thanks to structural analysis, today we know that the intracellular domains of TRPV ion channels, form
71 tetramers and that coupling between these domains regulates channel function (19, 23). In this context,
72 the overall nature of ARD interactions is poorly understood, but some evidences correlate with the
73 notion that they play a leading role in the functional mechanism of the channel (21, 24). For example,
74 there is some evidence of the ARD contributing to gating by selective oxidation of intracellular cysteines
75 present in the ARD (3, 25). Additionally, a complex formed by TRPV5 and calmodulin was solved
76 Recently (18). This interaction can be of interest since it also exists in TRPV1 and other members of the
77 family and it is located between C-termini and the ARD.

78 To further study the role of the ARD in TRPV1 we studied the integral relationships between ARD
79 function and channel gating. For this purpose, we employed coarse-grained molecular dynamics of the
80 whole TRPV1 channel embedded in a POPC/POPE membrane and also performed experiments with the
81 purified ARD in solution, making use of the thermal shift unfolding, circular dichroism, and tryptophan
82 fluorescence measurements. We find that the ARD is a dynamical domain and that these dynamics are
83 modulated by temperature in a way that might be relevant to activation by temperature.

84 Methods

85 Model Preparation

86 The cryo-electron microscopy (cryo-EM) structure of a minimal-functional rat TRPV1, solved at 3.4 Å
87 resolution, was used as initial coordinates to perform coarse-grained (CG) molecular dynamics (PDBID:
88 3J5P) (12). The missing loops and side chains were built in the Swiss Modeler web server (26, 27). To
89 generate our model, the server used the whole channel model (12) and the transmembrane cryo-EM
90 structure solved in nanodiscs (14). The repaired TRPV1 structure was prepared for coarse-graining by
91 means of the Martinize.py (28) program. A 20 nm per side, square POPC/POPE (coarse-grained)
92 membrane was prepared in CHARMM-GUI (29), the channel model was embedded into the membrane
93 using Pymol scripts written in-house. The TRPV1-POPC/POPE structure was prepared for molecular
94 dynamics (MD) simulation in the Gromacs 4.5 Suite (30, 31). The model was minimized and solvated
95 with CG water and surrounded by 30 mM NaCl ions. A 200 ns NVT equilibration dynamics with a
96 Berendsen Thermostat was performed before the production run (28, 30).

97 Structural comparison

98 Composite alignment was performed for cryo-EM models of open and closed states of TRPV1 and TRPV3
99 ion channels using the TopMatch Server (32). A blue to red gradient was used to represent root-mean
100 square deviation (RMSD) divergence in structural alignments. The Pymol module colorbyrmsd.py was
101 used for coloring.

102 Molecular Dynamics Simulations

103 We used coarse-grained molecular dynamics (CGMD) simulations to characterize the dynamics of the
104 ion channel in the membrane. We simulated the initially repaired APO model (PDBID: 3J5P) at various
105 temperatures varying from 290 K to 350 K (17 °C to 77 °C) sampling every 5 K. The structure of TRPV1
106 was embedded in a POPC/POPE bilayer with a MARTINI force field; several equilibrating simulations with
107 temperature coupling were performed, and then an equilibrating simulation with pressure and
108 temperature was performed until the RMSD was stable at 298 K (28). A production run at 290 K was
109 sampled as an initial structure. From a stable point in a 290 K run, thirteen replicas were prepared. The
110 RMSD corresponds to the mean of the whole protein main-chain over the whole simulation time and the
111 root-mean square fluctuation (RMSF) corresponds to the mean of a single amino acid position over time.
112 Both were calculated with Gromacs 4.5. The output trajectories were used as input for Normal Mode
113 Analysis (NMA). This analysis was performed in bio3D for the four subunits (33). Production runs were

114 performed in the “Miztli” HP Cluster Platform 3000SL supercomputer at the Supercomputing Facility of
115 the National Autonomous University of México (UNAM).

116 [ARD expression and purification](#)

117 The DNA sequence encoding for the ARD of rat TRPV1 (residues 100-262) was cloned into a pET28c
118 vector (Merck-Millipore, USA). For expression, the *Escherichia coli* BL21 (DE3) strain (NewEngland
119 Biolabs, USA) was transformed with this vector. Batch cultures of transformed cells were grown in Luria
120 Bertani broth (Sigma-Aldrich, USA) to an OD of 0.7-0.8, protein expression was then induced with
121 Isopropyl- β -D-1-thiogalactopyranoside 0.1 mM (GoldBio, Canada) for 12 h at room temperature. The cell
122 pellet was lysed in Tris 50 mM, pH 8, dithiothreitol 0.1 mM, NaCl 300 mM (Sigma-Aldrich, USA). The
123 lysate was purified by Histrap FF columns (GE Healthcare) with an imidazole gradient from 0 to 0.5 M.
124 The eluted protein was concentrated and desalted in a PD-10 column (GE Healthcare) against a Tris 50
125 mM, pH 8, dithiothreitol 0.1 mM buffer. Then, the protein was injected into a cation exclusion
126 chromatography column (MonoQ) and eluted against Tris 50 mM, pH 8, dithiothreitol 0.1 Mm buffer
127 with an increased linear gradient from 0-1 M of NaCl. The final step was a size exclusion
128 chromatography in a hand-made 275 mL Superdex 75 Column (Dimensions 2.50 x 60 cm, GE
129 Healthcare). ARD concentration was determined using a theoretical extinction coefficient of 1.21
130 L/mg-cm obtained using the ProtParam Expsy WebServer (34) and by bicinchoninic acid assays with
131 reduction compatible reagents (Pierce Chemicals, USA).

132 [Thermal Shift Unfolding](#)

133 Assays were prepared in a 96 well plate for real-time PCR; each well was prepared with 1 μ L of SYPRO
134 Dye 1X (Sigma-Aldrich, USA), 1 μ L of 1mg/mL solution of pure ARD, and 1 μ L of solubility and stability II
135 kit (Hampton Research, USA), water was added to fill 10 μ L per well. A real-time thermocycler
136 QuantStudio 3 (ThermoFisher, USA) was used for collecting data from 20 to 80 $^{\circ}$ C, sampling every 1 $^{\circ}$ C.
137 The data were exported and analyzed in IgorPro 6 (WaveMetrics, USA).

138 [Size Exclusion Chromatography - Multiple Angle Light Scattering \(SEC-MALS\)](#)

139 The SEC-MALS analysis was performed on a DAWN HELEOS multi-angle light scattering detector, with
140 eighteen angles detectors and a 658.9 nm laser beam, (Wyatt Technology, Santa Barbara, CA, USA) and
141 an Optilab T-rEX refractometer (Wyatt Technology) in-line with a Superdex 75 10/300 GL (GE Life
142 Sciences) size exclusion chromatography analytical column. Experiments were performed using an
143 isocratic pump (Agilent) with a flow of 0.5 ml/min at room temperature (25 $^{\circ}$ C). Data collection was

144 performed with ASTRA 6.1 software (Wyatt Technology). For the experiments, 300 μ l at 1 mg/ml protein
145 were loaded on the columns with running buffer of 20 mM glycine pH 9.5, 200 mM NaCl. The molecular
146 weight (MW) and the ratio of gyration (R_g) were calculated by the ASTRA software.

147 Circular Dichroism Spectroscopy

148 Circular dichroism (CD) spectroscopy was carried out in a JASCO J-715 spectropolarimeter with a 1 mm
149 path length cuvette, the sample was prepared at 250 μ g/mL in 5 mM sodium phosphate buffer. Samples
150 were heated at a 0.5 K min^{-1} rate with a Peltier device (JASCO). A thermal unfolding curve was generated
151 by measuring a spectrum for every step. CD data were analyzed in custom-made scripts and plotted with
152 Igor Pro 6 (WaveMetrics, USA). Normalized ellipticity data obtained at 208 nm were fitted to the
153 following sigmoid function to calculate the T_m :

$$154 \quad f(T) = \frac{1}{1 + e^{\left(\frac{T_m - T}{\text{slope}}\right)}} \quad \text{Equation 1}$$

155 Tryptophan Fluorescence Spectroscopy

156 Intrinsic fluorescence spectra were obtained in a PC1 spectrofluorometer (ISS Inc., USA) configured with
157 a 10 W halogen lamp as the excitation source. All samples were prepared at 50 μ g/L. Tryptophan
158 fluorescence spectra were obtained using an excitation wavelength of 295 nm, emission spectra were
159 collected from 310 to 400 nm, using excitation and emission slits of 0.25 and 1 mm respectively. The
160 temperature was controlled with a Peltier device (Quantum Northwest). Normalized intensity at 330 nm
161 and SCM data (see below) were fitted to Eq. 1.

162 The fluorescence spectral center of mass (SCM) was obtained from each spectrum and plotted as a
163 function of temperature. The SCM was calculated from intensity data (I_λ) obtained at different
164 wavelengths (λ). $SCM = \frac{\sum \lambda \cdot I_\lambda}{\sum I_\lambda}$

165 Results

166 Cytosolic domains of TRPV1 fluctuate more at higher temperature

167 It is generally assumed that TRPV1 is formed by a cluster of functional domains (Fig 1c), each with a set
168 of specific interactions. The ARD, MPD and TRP-Box domains are intracellular. Several groups have found
169 that the minimal functional TRPV1 structure needs the N-termini from the ANK1 motif upwards (12, 20,

170 35) and no more than one hundred amino acids from the C-terminus can be deleted without rendering
171 the channel non-functional (35) .

172 As an initial point in our research to understand the behavior of TRPV1 as a function of temperature, we
173 carried out coarse-grain molecular dynamics simulations at different temperatures using a full-length
174 model of TRPV1 embedded in a phosphatidylcholine/phosphatidylethanolamine (POPC/POPE) lipid
175 membrane (Fig. 1a). The initial model was derived from the closed TRPV1 structure (PDBID: 3J5P) solved
176 by cryo-EM (12). The model was simulated for 200 ns in temperature-controlled conditions (NVT) for
177 stabilization and then 200 ns of pressure and temperature controlled conditions (NPT) with Berendsen
178 thermostat and pressure coupling (see Methods). The simulations were equilibrated until the channel
179 was in a stable RMSD state, from that point on, 12 replicas were simulated at 290, 295, 300, 305, 310,
180 315, 320, 325, 330, 335, 340, 345 and 350 K. At these temperatures independent runs of 500 ns were
181 simulated to sample for an adequate time in order to observe critical large-scale structural transitions.

182 In figure 1b, we represent the RMSF of a single subunit of the whole TRPV1 tetramer. Temperatures
183 from 290 to 350 K were sampled and averaged; each point is the average of RMSF of a particular residue
184 for all the temperatures. The variance (s^2) of the mean RMSF is plotted as a measure of dispersion from
185 0 to 0.26. The mean RMSF for all the subunit is 0.27 ± 0.22 ; 0.45 ± 0.21 for the ARD and 0.40 ± 0.21 for
186 the ARD + MPD. The RMSF deviation, which correlates the fluctuation per amino acid during the
187 trajectory of the dynamics, shows that there are some regions that fluctuate more than others as the
188 temperature is increased. The regions with well-defined secondary structure have less movement and
189 the loops and less structured chains move more (Figure 1b). The transmembrane region of the channel
190 has smaller magnitude movements in relation to the cytosolic part; this is likely due to the two-
191 dimensional restriction of the lipid membrane. Interestingly, the data shows that the mean RMSF greatly
192 increases in the N and C-termini, even though these are regions with well-defined secondary structure.

193 All the N-terminus (ARD + MPD) shows a significant increase in main movement as temperature rises.
194 The ankyrin motifs (ANK) are represented in Fig 1a. ANK1 and ANK2 are not solved in the cryo-EM
195 structure (Supplemental Fig. 1c) and in our analysis these repeats presented a large average RMSF of
196 0.66 and the highest variance per amino acid, above 0.20. While the C-terminus also has a high value of
197 temperature-dependent RMSF, for the purpose of this study, it will not be discussed.

198 Protein dynamics and inter-subunit interactions of TRPV1

199 In order to study the coarse-grained dynamics of TRPV1 and provide a quantitative interpretation of the
200 simulations, we performed normal mode analysis (NMA), (36, 37). We identified a first mode in which
201 the ARDs undergo alternate up-and-down movements. Figure 2a and b shows the structure at two
202 different stages of the oscillation. The arrows indicate the direction of the movement of each of the
203 coarse-grained beads. The bottom panels show a view from the intracellular region of the channel. This
204 normal mode represents more than 70% of the movements of each trajectory and this is seen at all the
205 simulated temperatures.

206 Fluctuation analyses were performed from the trajectories by means of the greater NMA eigenvectors
207 (33). Figure 2c shows the fluctuation analysis of the 290 K trajectory depicted from the same normal
208 mode from 2a and 2b. It can be seen that the highest values of the fluctuations occur at the ankyrin
209 repeats one and two and the fluctuations extend into the whole ARD.

210 A deformation displacement analysis was performed from the NMA; this is obtained by the averaged
211 values of each individual mode, and by measuring the contribution of each backbone bead to the energy
212 density as a function of position (36). This analysis provides information on the correlation between
213 regions with high deformation and regions that are most affected by this deformation. Figure 2d shows
214 that the regions with higher deformation are the ARD and that the regions with highest correlation with
215 the deformation of the ARD is the MPD. This is a reflection of the physical interactions between these
216 two domains but also means that the conformational changes in one domain are transmitted to the
217 other in the interaction pair.

218 Comparison of Molecular Dynamics Trajectory with CryoEM Structures

219 The structures of closed and open TRPV1 were compared by means of composite alignment. In contrast
220 to rigid body alignment, this method allows the part-by-part alignment leaving out the regions without
221 structural match.

222 The structure of TRPV1 in the apo, closed-like state (PDBID: 2J5P), the capsaicin-bound (CB) structure
223 (PDBID: 2J5R) and an open-like structure bound to the activating double-knot toxin (DkTx) and
224 resiniferatoxin (RTX) (PDBID: 2J5Q), were analyzed. First, the published DkTx/RTX toxin-bound structure
225 (TXB) has a selectivity filter in an expanded open conformation (13) while the CB structure only shows
226 an increase in the diameter of the lower gate (12, 13) (Supplemental figure 2). The closed-like
227 conformation has similarity with both TXB and CB structures; in supplemental figure 2 we show that the

228 closed structure is similar to CB in the upper part of transmembrane domain, as well as in the selectivity
229 filter. The TXB structure has a wide-open selectivity filter but this structure is similar in the lower part of
230 the transmembrane domain, S6 helix and TRP-box domain to the CB structure. TRPV3 closed (PDBID:
231 6DVW) and open (PDBID: 6DVY) structures were also analyzed for comparison (Supplemental Fig 2c).
232 The composite alignment of open vs. closed TRPV3 is closer to CB-TRPV1 vs. closed TRPV1 (23),
233 (Supplemental Fig 2a and 2c). Closed TRPV1 and open TRPV3 are not comparable, but the composite
234 alignment between structures has many similarities and importantly the ARD domain presents a high
235 RMSD.

236

237 [The conformation of the ARD shows a thermal dependency at physiological temperature.](#)

238 The simulation data illustrates that the intracellular domains of TRPV1 undergo conformational changes
239 at temperatures that are relevant to the physiological activation of the channel. The region that shows
240 the largest mobility is the ARD, a 260 amino acid region in the N-terminus of TRPV channels. In TRPV1,
241 the ARD is implicated in adenosine triphosphate binding, Ca^{2+} -calmodulin modulation and regulation by
242 cysteine oxidation (3, 21, 25, 38). In the whole channel, the ARD has several complex interactions with
243 the pre-S1 region (MPD, 90 amino acids) in the same subunit, and a characteristic ARD-MPD interaction
244 with the adjacent subunit (Fig 1a and 1c) (12). The ARD also has an interaction with the distal C-
245 terminus, this region is not well solved in TRPV1 cryo-EM structure but in TRPV2 and TRPV3 it is (15, 16).
246 The functional significance of these interactions remains unknown.

247 As a first approximation to study the biophysical properties of the N-terminus, we purified an ARD from
248 rTRPV1 and screened its stability by a thermal shift assay (Figure 3), utilizing several pH and salt
249 concentration conditions (see Methods). Figure 3a shows the fluorescence signal from the dye SYPRO
250 orange as a reporter of the thermal unfolding process. SYPRO emits a fluorescence signal by binding to
251 hydrophobic regions exposed during unfolding. The fluorescence signals show a characteristic sigmoid
252 dependence on temperature, which is a feature of a two-state unfolding process in soluble proteins. To
253 characterize the cooperativity of the change in fluorescence, the first derivative was calculated for every
254 trace (Fig. 3a, 3b and 3c).

255 The data show that the first derivative of the fluorescence increases linearly as a function of pH. The
256 data in Figure 3a, inset, indicate that the cooperativity of the unfolding of the ARD is highest at basic pH,
257 as the value of the derivative increases as pH increases. The inset in Fig. 3b shows that additionally to

258 the increased cooperativity, the domain becomes more stable, since the T_m value, defined as the
259 temperature at which the derivative is maximal, shifts to higher temperatures. Next, the dependence on
260 salt concentration was analyzed for the pH 9.5 condition. In Figure 3c we show the data for glycine
261 buffer (pH 9.5) and several NaCl concentrations. The steepness of the fluorescence change is higher at
262 low salt concentrations and the T_m decreases with increasing salt concentration, with a slope of -0.05
263 and a change in T_m from 36 to 38 °C. The behavior of ARD in glycine buffer (pH 9.5) was also studied by
264 SEC-MALS to control for its possible oligomeric assembly. The experiment shows that the ARD is
265 monodisperse in these conditions (Supplementary figure 3).

266 Significantly, these series of experiments indicate that the thermal transitions of the isolated ARD occur
267 in a range of temperatures that is rather narrow ($T_m = 36-38$ °C for the most stable condition) and very
268 close to the physiological temperature of mammals.

269

270 [Stability of the ARD in solution](#)

271 Since SYPRO thermal shifts are mostly qualitative, we compared the thermal sensitivity of the ARD by
272 means of tryptophan fluorescence and circular dichroism (CD) experiments. Figure 4a shows far-UV CD
273 spectra (200 to 240 nm) of ARD obtained at increasing temperatures (see methods for details). The CD
274 spectrum at 25°C is consistent with the high alpha helical content of the ARD structure. The shape and
275 ellipticity of individual spectra changes as temperature is increased, indicating the presence of thermal
276 unfolding of the ARD.

277 Since the main CD signal is due to a macro dipole formed by the sum of dipoles of all the secondary
278 structures, the decrease of ellipticity is characteristic of a random array of secondary structures, even
279 when a single alpha helix does not have zero signal. In the case of the ARD, the loss of signal can be
280 associated to an increase of mobility between motifs. To characterize the change in CD, we normalized
281 the signal at 208 nm and plotted it as a function of temperature (Fig. 4b). The unfolding occurs with a
282 very steep dependence on temperature, with a T_m of ~34 °C, which is in agreement with the T_m observed
283 in the thermal shift experiments. We attempted to measure the reversibility of the unfolding reaction;
284 this result is plotted as blue circles in figure 4b and shows that thermal unfolding of the ARD is
285 irreversible. In comparison, the closest ARD previously studied is from the hTRPV4, which has a T_m of
286 37.1 °C measured by CD but its reversibility was not tested (38).

287 Thermal unfolding was also measured by tryptophan fluorescence experiments. The ARD has an
288 exposed Trp at position 272 of the ANK4 repeat. Excitation of this Trp at 295 nm and measurement of
289 the fluorescence at 330 nm as a function of increasing temperature shows an increase in the
290 fluorescence counts (Fig. 4c). The fluorescence increases (dequenching) in a temperature dependent
291 manner and a sigmoid function was fitted with a T_m of 39.7 °C (Fig 4d). A more robust analysis of Trp
292 fluorescence dequenching is provided by a spectral center of mass analysis (SCM), which takes into
293 account the contribution of the whole emission spectrum (39). This analysis is shown in the inset in
294 figure 4d and indicates that the T_m value obtained from the fit is T_m of 34.9 °C, which is closer to the T_m
295 obtained from the CD experiments.

296 Discussion

297 A defining characteristic of TRPV and other thermoTRP channels is the presence of several ankyrin
298 repeats in the N-terminus. Elucidation of their functional role has been a main objective of TRP channel
299 structure function studies. Others ARDs from different proteins show a variety of functions, from
300 replication/translation regulation to protein-protein interaction and ligand binding (40–42).

301 TRPV1 is one of the best-studied members of the thermoTRP channel subfamily. Notwithstanding the
302 wealth of available information, the mechanisms of heat sensitivity and heat-dependent activation
303 remain poorly understood. Several mechanisms of thermal sensing have been proposed: The
304 transmembrane regions could contribute with a significant heat capacity and serve as a thermal sensor
305 domains (43); the pore domain could act as a temperature sensing domain (44) and the intracellular
306 and transmembrane domains could act cooperatively to contribute to thermal sensation through a
307 mechanism involving a linker domain (22). In TRPA1 channels, the ARD, although much bigger than the
308 TRPV1 ARDs, have been implicated in temperature sensation.

309 Several TRPV1 structures determined by cryo-EM exist and are useful in interpreting experiments and
310 proposing new ones, but the quality of these structures is in general poor. All of them are missing
311 electronic density that should correspond to the initial ankyrin repeats of the ARD. Possible reasons for
312 this are: high density of side chain of the amino acids, presence of salt bridges or the loss of density near
313 Asp and Glu residues (45). Another possibility is higher mobility of this whole region of the protein
314 structure (Supplemental figure 1). Our coarse-grain MD simulations with a repaired model show that
315 indeed the amino terminus and, in particular the ARD, are highly dynamic regions. An important result
316 stemming from these simulations is that increased temperatures also modulate the high mobility of

317 ARDs. Experimentally, deletion of the ARD results in non-functional TRPV1 channels (12, 35), a result
318 that has hindered an understanding of the role of ARs in heat sensitivity and other forms of gating in this
319 channel. The ARDs are responsible for auto recognition, and probably an auto modulation mechanism
320 by self-interaction.

321 Our approach identifies the dynamics of the ARD of TRPV1 as important for the overall function of the
322 ion channel. The low frequency movement represented by the first normal mode identified in this study,
323 suggest that the ARD is a dynamical module that might contribute to the response of TRPV1 to
324 temperature. We propose that these fluctuations might be important in controlling temperature
325 dependent gating of TRPV1. At the very least, our results highlight the importance of the ARD and its
326 interactions with other parts of the channel in regulating channel gating.

327 The structure of the ARD of TRPV1 was previously solved by crystallography (46). Lishko et al. also
328 showed that basic pH is better for ARD purification (46). Also, there are some groups that report a brief
329 activation of the functional TRPV1 at basic pH (47).

330 Our data from CGMD simulations support a highly dynamical conformation of the ARD, and show
331 breaking of some contacts between the second and third AR motifs at higher temperatures. This kind of
332 perturbations may decrease stability of ARD as illustrated by the unfolding experiments in designed
333 ARDs (40, 48) and might contribute to a conformational change coupled to channel opening.

334 Our biochemical data provide experimental support for the fluctuations observed in the simulations.
335 Importantly, we observe conformational changes in the structure of the isolated ARD that occur at
336 physiologically relevant temperatures. Our results indicate that the structure of the ARD undergoes
337 important changes over a range of $\sim 25^{\circ}\text{C}$. The CD data indicates that at 50°C the structure is highly
338 altered, but still contains a significant amount of alpha-helical structure. This result might indicate that
339 the ARD is not completely unfolded into a random coil. An important observation is the fact that this
340 structure is not reversible. In accordance with this, we have recently shown that temperature-
341 dependent gating of full length TRPV1 is also irreversible and this irreversibility is reflected in a large
342 hysteresis during the activation processes (49). It is thus possible that the behavior of the ARD observed
343 here could be related to this irreversible gating process.

344 Some naturally occurring splicing variants of TRPV1 have been described. The ARD and MPD are part of
345 two different exons, and the splicing variants ARD-less and MPD-less express ion channels that are not
346 sensitive to temperature (50). In our simulations and structural analysis, it is observed that the distal

347 ARD (ANK1-2) approaches the MPD domain. This interaction is hard to measure by MD because it is
348 known that in this region a C terminal peptide forms a third beta strand of the MPD finger loop. Our
349 analysis of the correlations of fluctuation during a simulated trajectory also highlights this interaction.
350 Our data derived from NMA indicate that the regions that show highest correlated movement are
351 precisely the proximal ARD and the MPD.

352 The importance of the ARD-MPD interaction in TRPV1 function is also highlighted by experiments by Yao
353 et al., in which several TRPV1-MPD chimaeras were generated between rTRPV2, hTRPV2, mTRPV3 and
354 mTRPV4. All the chimeras increased the sensitivity to temperature. These results are consistent with the
355 ARD being in direct contact with the adjacent MPD, in such a way that its ability to interact with a viable
356 MPD might play a role in the capacity of the TRPV channels to being thermally sensitive.

357 In conclusion, structure-function studies and natural occurring variants of the N-terminus (ARD + MPD)
358 support its fundamental role for TRPV1 function. Our study contributes to an understanding of the
359 dynamics of ARD and suggests that it participates in the regulation of thermal sensing, although its
360 function as a thermal sensor or an element in temperature coupling remains to be elucidated.

361

362 Author's contributions

363 E. L-de-G, Designed experiments, performed experiments and simulations, analyzed data and wrote
364 paper. G. E. R-Y, contributed materials, performed molecular biology and read the paper. D. A. F-V,
365 helped with CD and fluorescence experiments, read the paper and analyzed data. A. T-L, helped with
366 SECS-MALS and thermal shift experiments, read the paper and analyzed data. T. R., designed
367 experiments and wrote the paper. L. D. Islas, Designed experiments, analyzed data and wrote the paper.

368 Conflict of Interest

369 The authors declare no conflict of interest.

370 Acknowledgments

371 E. Ladrón-de-Guevara is grateful to Consejo Nacional de Ciencia y Tecnología (CONACYT) for a PhD
372 scholarship (grant no. 297659). We acknowledge support from DGAPA-PAPIIT grant No. IN209515 to
373 L.D.I and No. IN200717 to T.R. We also acknowledge support from CONACyT-Ciencia Básica grant No.
374 252644 to L.D.I and No. A1-S-8760 to T.R. We are specially grateful with Dirección General de Cómputo

375 y de Tecnologías de Información y Comunicación (DGTIC-UNAM) project LANCAD-UNAM-DGTIC-290 for
376 use of the Miztli Supercomputer.
377

378 References

- 379 1. Aneiros, E., L. Cao, M. Papakosta, E.B. Stevens, S. Phillips, and C. Grimm. 2011. The biophysical
380 and molecular basis of TRPV1 proton gating. *EMBO J.* 30: 994–1002.
- 381 2. Caterina, M.J., M.A. Schumacher, M. Tominaga, T.A. Rosen, J.D. Levine, and D. Julius. 1997. The
382 capsaicin receptor: A heat-activated ion channel in the pain pathway. *Nature.* 389: 816–824.
- 383 3. Salazar, H., I. Llorente, A. Jara-Oseguera, R. Garcia-Villegas, M. Munari, S.E. Gordon, L.D. Islas, and
384 T. Rosenbaum. 2008. A single N-terminal cysteine in TRPV1 determines activation by pungent
385 compounds from onion and garlic. *Nat. Neurosci.* 11: 255–261.
- 386 4. Pingle, S.C., J. a. Matta, and G.P. Ahern. 2007. Capsaicin receptor: TRPV1 a promiscuous TRP
387 channel. *Handb. Exp. Pharmacol.* 179: 155–171.
- 388 5. Yarmolinsky, D.A., Y. Peng, L.A. Pogorzala, M. Rutlin, M.A. Hoon, and C.S. Zuker. 2016. Coding and
389 Plasticity in the Mammalian Thermosensory System. *Neuron.* 92: 1079–1092.
- 390 6. Caterina, M.J., A. Leffler, A.B. Malmberg, W.J. Martin, J. Trafton, K.R. Petersen-Zeitz, M.
391 Koltzenburg, A.I. Basbaum, and D. Julius. 2000. Impaired nociception and pain sensation in mice
392 lacking the capsaicin receptor. *Science.* 288: 306–13.
- 393 7. Huang, S.M., X. Li, Y. Yu, J. Wang, and M.J. Caterina. 2011. TRPV3 and TRPV4 ion channels are not
394 major contributors to mouse heat sensation. *Mol. Pain.* 7: 37.
- 395 8. Park, U., N. Vastani, Y. Guan, S.N. Raja, M. Koltzenburg, and M.J. Caterina. 2011. TRP vanilloid 2
396 knock-out mice are susceptible to perinatal lethality but display normal thermal and mechanical
397 nociception. *J. Neurosci.* 31: 11425–36.
- 398 9. Iida, T., I. Shimizu, M.L. Nealen, A. Campbell, and M. Caterina. 2005. Attenuated fever response in
399 mice lacking TRPV1. *Neurosci. Lett.* 378: 28–33.
- 400 10. Nieto-Posadas, A., G. Picazo-Juárez, I. Llorente, A. Jara-Oseguera, S. Morales-Lázaro, D. Escalante-
401 Alcalde, L.D. Islas, and T. Rosenbaum. 2011. Lysophosphatidic acid directly activates TRPV1

- 402 through a C-terminal binding site. *Nat. Chem. Biol.* 8: 78–85.
- 403 11. Ufret-Vincenty, C.A., R.M. Klein, M.D. Collins, M.G. Rosasco, G.Q. Martinez, and S.E. Gordon.
404 2015. Mechanism for phosphoinositide selectivity and activation of TRPV1 ion channels. *J. Gen.*
405 *Physiol.* 145: 431–42.
- 406 12. Liao, M., E. Cao, D. Julius, and Y. Cheng. 2013. Structure of the TRPV1 ion channel determined by
407 electron cryo-microscopy. *Nature.* 504: 107–12.
- 408 13. Cao, E., M. Liao, Y. Cheng, and D. Julius. 2013. TRPV1 structures in distinct conformations reveal
409 activation mechanisms. *Nature.* 504: 113–8.
- 410 14. Gao, Y., E. Cao, D. Julius, and Y. Cheng. 2016. TRPV1 structures in nanodiscs reveal mechanisms of
411 ligand and lipid action. *Nature.* 534: 347–51.
- 412 15. Zubcevic, L., M.A. Herzik, B.C. Chung, Z. Liu, G.C. Lander, and S.Y. Lee. 2016. Cryo-electron
413 microscopy structure of the TRPV2 ion channel. *Nat. Struct. Mol. Biol.* 23: 180–186.
- 414 16. Zubcevic, L., M.A. Herzik, M. Wu, W.F. Borschel, M. Hirschi, A.S. Song, G.C. Lander, and S.-Y. Lee.
415 2018. Conformational ensemble of the human TRPV3 ion channel. *Nat. Commun.* 9: 4773.
- 416 17. Deng, Z., N. Paknejad, G. Maksaev, M. Sala-Rabanal, C.G. Nichols, R.K. Hite, and P. Yuan. 2018.
417 Cryo-EM and X-ray structures of TRPV4 reveal insight into ion permeation and gating
418 mechanisms. *Nat. Struct. Mol. Biol.* 25: 252–260.
- 419 18. Hughes, T.E.T., R.A. Pumroy, A.T. Yazici, M.A. Kasimova, E.C. Fluck, K.W. Huynh, A. Samanta, S.K.
420 Molugu, Z.H. Zhou, V. Carnevale, T. Rohacs, and V.Y. Moiseenkova-Bell. 2018. Structural insights
421 on TRPV5 gating by endogenous modulators. *Nat. Commun.* 9: 4198.
- 422 19. McGoldrick, L.L., A.K. Singh, K. Saotome, M. V. Yelshanskaya, E.C. Twomey, R.A. Grassucci, and
423 A.I. Sobolevsky. 2018. Opening of the human epithelial calcium channel TRPV6. *Nature.* 553:
424 233–237.
- 425 20. De-la-Rosa, V., G.E. Rangel-Yescas, E. Ladrón-de-Guevara, T. Rosenbaum, and L.D. Islas. 2013.
426 Coarse architecture of the transient receptor potential vanilloid 1 (TRPV1) ion channel
427 determined by fluorescence resonance energy transfer. *J. Biol. Chem.* 288: 29506–17.
- 428 21. Rosenbaum, T., A. Gordon-Shaag, M. Munari, and S.E. Gordon. 2004. Ca²⁺/calmodulin modulates
429 TRPV1 activation by capsaicin. *J. Gen. Physiol.* 123: 53–62.

- 430 22. Yao, J., B. Liu, and F. Qin. 2011. Modular thermal sensors in temperature-gated transient
431 receptor potential (TRP) channels. *Proc. Natl. Acad. Sci. U. S. A.* 108: 11109–14.
- 432 23. Singh, A.K., L.L. McGoldrick, and A.I. Sobolevsky. 2018. Structure and gating mechanism of the
433 transient receptor potential channel TRPV3. *Nat. Struct. Mol. Biol.* 25: 805–813.
- 434 24. Kasimova, M.A., A. Yazici, Y. Yudin, D. Granata, M.L. Klein, T. Rohacs, and V. Carnevale. 2018. Ion
435 Channel Sensing: Are Fluctuations the Crux of the Matter? *J. Phys. Chem. Lett.* 9: 1260–1264.
- 436 25. Chuang, H., and S. Lin. 2009. Oxidative challenges sensitize the capsaicin receptor by covalent
437 cysteine modification. *Proc. Natl. Acad. Sci. U. S. A.* 106: 20097–102.
- 438 26. Waterhouse, A., M. Bertoni, S. Bienert, G. Studer, G. Tauriello, R. Gumienny, F.T. Heer, T.A.P. de
439 Beer, C. Rempfer, L. Bordoli, R. Lepore, and T. Schwede. 2018. SWISS-MODEL: homology
440 modelling of protein structures and complexes. *Nucleic Acids Res.* 46: W296–W303.
- 441 27. Bordoli, L., and T. Schwede. 2012. Automated protein structure modeling with SWISS-MODEL
442 Workspace and the Protein Model Portal. *Methods Mol. Biol.* 857: 107–36.
- 443 28. de Jong, D.H., G. Singh, W.F.D. Bennett, C. Arnarez, T.A. Wassenaar, L. V. Schäfer, X. Periole, D.P.
444 Tieleman, and S.J. Marrink. 2013. Improved Parameters for the Martini Coarse-Grained Protein
445 Force Field. *J. Chem. Theory Comput.* 9: 687–97.
- 446 29. Hsu, P.-C., B.M.H. Bruininks, D. Jefferies, P. Cesar Telles de Souza, J. Lee, D.S. Patel, S.J. Marrink,
447 Y. Qi, S. Khalid, and W. Im. 2017. CHARMM-GUI Martini Maker for modeling and simulation of
448 complex bacterial membranes with lipopolysaccharides. *J. Comput. Chem.* 38: 2354–2363.
- 449 30. Pronk, S., S. Páll, R. Schulz, P. Larsson, P. Bjelkmar, R. Apostolov, M.R. Shirts, J.C. Smith, P.M.
450 Kasson, D. van der Spoel, B. Hess, and E. Lindahl. 2013. GROMACS 4.5: a high-throughput and
451 highly parallel open source molecular simulation toolkit. *Bioinformatics.* 29: 845–54.
- 452 31. Van Der Spoel, D., E. Lindahl, B. Hess, G. Groenhof, A.E. Mark, and H.J.C. Berendsen. 2005.
453 GROMACS: fast, flexible, and free. *J. Comput. Chem.* 26: 1701–18.
- 454 32. Sippl, M.J., and M. Wiederstein. 2012. Detection of spatial correlations in protein structures and
455 molecular complexes. *Structure.* 20: 718–28.
- 456 33. Grant, B.J., A.P.C. Rodrigues, K.M. ElSawy, J.A. McCammon, and L.S.D. Caves. 2006. Bio3d: An R
457 package for the comparative analysis of protein structures. *Bioinformatics.* 22: 2695–2696.

- 458 34. Gasteiger, E., C. Hoogland, A. Gattiker, S. Duvaud, M.R. Wilkins, R.D. Appel, and A. Bairoch. 2005.
459 Protein Identification and Analysis Tools on the ExpASY Server. In: *The Proteomics Protocols*
460 *Handbook*. Totowa, NJ: Humana Press. pp. 571–607.
- 461 35. Hellwig, N., N. Albrecht, C. Harteneck, G. Schultz, and M. Schaefer. 2005. Homo- and heteromeric
462 assembly of TRPV channel subunits. *J. Cell Sci.* 118: 917–28.
- 463 36. Hinsen, K. 1998. Analysis of domain motions by approximate normal mode calculations. *Proteins.*
464 33: 417–29.
- 465 37. Skjaerven, L., S.M. Hollup, and N. Reuter. 2009. Normal mode analysis for proteins. *J. Mol. Struct.*
466 *THEOCHEM.* 898: 42–48.
- 467 38. Inada, H., E. Procko, M. Sotomayor, and R. Gaudet. 2012. Structural and biochemical
468 consequences of disease-causing mutations in the ankyrin repeat domain of the human TRPV4
469 channel. *Biochemistry.* 51: 6195–6206.
- 470 39. Ruan, K., and G. Weber. 1989. Hysteresis and conformational drift of pressure-dissociated
471 glyceraldehydephosphate dehydrogenase. *Biochemistry.* 28: 2144–53.
- 472 40. Ferreiro, D.U., C.F. Cervantes, S.M.E. Truhlar, S.S. Cho, P.G. Wolynes, and E.A. Komives. 2007.
473 Stabilizing $\text{IkappaB}\alpha$ by “consensus” design. *J. Mol. Biol.* 365: 1201–16.
- 474 41. Barrick, D., D.U. Ferreiro, and E.A. Komives. 2008. Folding landscapes of ankyrin repeat proteins:
475 experiments meet theory. *Curr. Opin. Struct. Biol.* 18: 27–34.
- 476 42. Mosavi, L.K., T.J. Cammett, D.C. Desrosiers, and Z.-Y. Peng. 2004. The ankyrin repeat as molecular
477 architecture for protein recognition. *Protein Sci.* 13: 1435–1448.
- 478 43. Chowdhury, S., B.W. Jarecki, and B. Chanda. 2014. A molecular framework for temperature-
479 dependent gating of ion channels. *Cell.* 158: 1148–1158.
- 480 44. Zhang, F., A. Jara-Oseguera, T.-H. Chang, C. Bae, S.M. Hanson, and K.J. Swartz. 2018. Heat
481 activation is intrinsic to the pore domain of TRPV1. *Proc. Natl. Acad. Sci. U. S. A.* 115: E317–E324.
- 482 45. Hryc, C.F., D.-H. Chen, P. V. Afonine, J. Jakana, Z. Wang, C. Haase-Pettingell, W. Jiang, P.D. Adams,
483 J.A. King, M.F. Schmid, and W. Chiu. 2017. Accurate model annotation of a near-atomic
484 resolution cryo-EM map. *Proc. Natl. Acad. Sci. U. S. A.* 114: 3103–3108.

- 485 46. Lishko, P. V., E. Procko, X. Jin, C.B. Phelps, and R. Gaudet. 2007. The Ankyrin Repeats of TRPV1
486 Bind Multiple Ligands and Modulate Channel Sensitivity. *Neuron*. 54: 905–918.
- 487 47. Dhaka, A., V. Uzzell, A.E. Dubin, J. Mathur, M. Petrus, M. Bandell, and A. Patapoutian. 2009.
488 TRPV1 is activated by both acidic and basic pH. *J. Neurosci*. 29: 153–8.
- 489 48. Parra, R.G., R. Espada, N. Verstraete, and D.U. Ferreira. 2015. Structural and Energetic
490 Characterization of the Ankyrin Repeat Protein Family. *PLoS Comput. Biol.* 11: e1004659.
- 491 49. Sanchez-Moreno, A., E. Guevara-Hernandez, R. Contreras-Cervera, G. Rangel-Yescas, E. Ladron-
492 de-Guevara, T. Rosenbaum, and L.D. Islas. 2018. Irreversible temperature gating in *trpv1* sheds
493 light on channel activation. *Elife*. : 251124.
- 494 50. Schumacher, M.A., I. Moff, S.P. Sudanagunta, and J.D. Levine. 2000. Molecular cloning of an N-
495 terminal splice variant of the capsaicin receptor. Loss of N-terminal domain suggests functional
496 divergence among capsaicin receptor subtypes. *J. Biol. Chem.* 275: 2756–62.

497

498 Figure legends

499

500 **Figure 1.** Depiction of the all-atom model of TRPV1, derived from the 3J5P PDB structure. (a, left), side
501 view of TRPV1. The coloring of its domains is as follow: ARD, violet; MPD, yellow; VSD, cyan; PD, blue
502 TRP-box, red. The bilayer is represented as spheres. (a, right), the intracellular view of the channel is
503 represented with the same coloring code. Inter-subunit interactions are seen between MPD and ARD.
504 (b) Analysis of the structural fluctuations induced by temperature by RMSF of the beads that correspond
505 to main chain of each amino acid in coarse-grained MD. Averaged values were plotted as black dots. The
506 discontinuity in the PD corresponds to the turret loop, which is not resolved in the cryo-EM structure.
507 The ankyrin motifs have the greatest variance and RMSF are ANK1 and ANK2. All the ankyrin motifs are
508 numbered from 1-6. (c) Single subunit depiction, voltage sensor-like domain (VSD) and pore domain (PD)
509 are membrane embedded domains, ARD is fully cytosolic. The membrane proximal domain (MPD) has
510 complex interactions with ARD, VSD, TRP-box. The TRP-box is sandwiched between the MPD and VSD.

511 **Figure 2.** Normal mode analysis of TRPV1. The 290 K trajectory was analyzed to obtain normal modes. (a
512 and b) The first mode shows an alternating upwards and downwards movement of adjacent ARDs. The

513 red arrows indicate the direction of movement. The subunits are numbered for clarity. (a) Domains 1
514 and 3 moved downwards while 2 and 4 are upwards. (b) Opposed domains moved upwards (1 and 3)
515 and downwards (2 and 4). The bottom panels show the intracellular view of the channel after a 90 °
516 rotation. (c) Fluctuations calculated by RMSF per bead relative to main chain. ARDs show the highest
517 values of fluctuations. Bottom panel, view of a 90° rotation of the channel. The scale represents the
518 value of the calculated fluctuation. (d) Deformation values of motion relative to neighbors. The MPDs
519 show the highest correlated movement with the ARD (pink color). The values were calculated with Bio3d
520 (see methods), (33, 36). The scale represents the calculated deformation values. The proximal ARD
521 (ANK3 to MPD) was highly correlated.

522 **Figure 3.** Thermal shift unfolding of ARD. (a) Representative raw SYPRO fluorescence signals obtained in
523 a real time thermocycler are plotted as a function of temperature. The lower panel shows the first
524 derivative of each signal. (b) First derivative (FD) plot (A.U./°C) of similar data as in (a) obtained at
525 different pH values. The melting temperature, T_m , was calculated as the temperature where the
526 maximum occurs. Inset shows the T_m of the ARD at different pH values. (c) Melting temperature T_m of
527 ARD in glycine buffer (pH 9.5) at different sodium chloride concentration. The inset shows the
528 dependence of T_m on the NaCl concentration.

529 **Figure 4.** Thermal stability of ARD. (a) CD spectra of the ARD at the temperatures indicated in the inset f.
530 (b) The normalized ellipticity change at 208 nm is plotted as a function of temperature. Data are mean
531 and s.e.m. for $n = 3$ experiments (black circles). The blue circles are the data from one experiment at an
532 attempt at refolding of the ARD by returning the temperature to 30 °C and indicate an irreversible
533 unfolding transition. The continuous curve represents a fit to a sigmoid function (slope 1.13 ± 0.14). The
534 value of T_m from the fit is of $34.2 \text{ °C} \pm 0.2 \text{ °C}$. (c) Tryptophan fluorescence spectra of the ARD at the
535 temperatures indicated by the color scale. (d) The normalized fluorescence intensity increase for $n = 3$
536 experiments is plotted as the mean \pm s.e.m. The continuous curve represents a fit to a sigmoid function
537 (slope 2.17 ± 0.10). The value of T_m from the fit of intensity data is $39.7 \text{ °C} \pm 0.1 \text{ °C}$. The SCM analysis is
538 shown in the inset. The parameters of the SCM fit are: slope 3.69 ± 0.13 and a T_m $35.0 \pm 0.2 \text{ °C}$.

539 **Supplemental Figure 1.** Quality of TRPV1 cryo-EM structures and crystallographic structure of ARD. (a)
540 Side view of the missing occupancies of side chain atoms in the capsaicin-bound (CB) structure, PDBID:
541 2J5R. Orange spheres indicate the amino acids where the electronic density is not seen and the heavy
542 atoms are not described; a representation by spheres shows the amino acids missing in the structure.
543 Bottom view of the CB structure showing missing atoms in the cryo-EM structure. (b) Missing

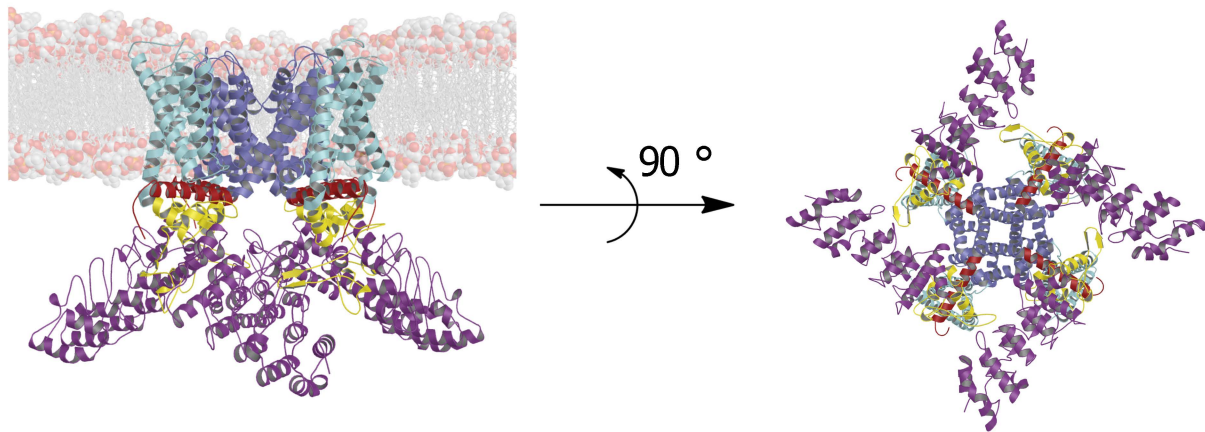
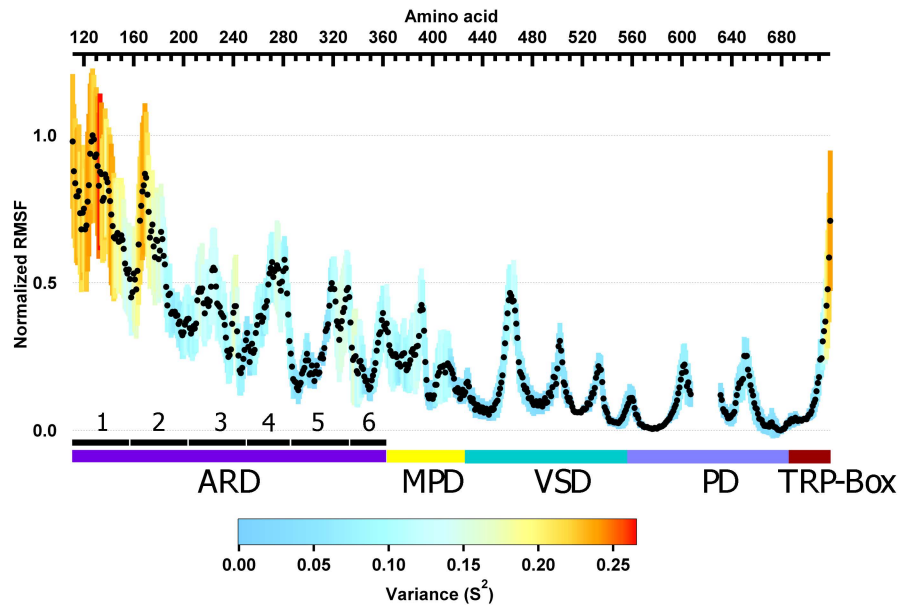
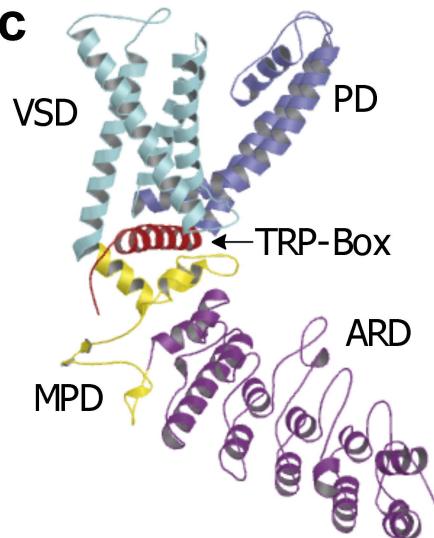
544 occupancies in the APO structure (3J5P), the missing occupancies vs. the CB structure are represented;
545 the APO structure is a reliable model for coarse-grained MD. (c) Ankyrin motifs 1 (ANK1) and 2 (ANK2)
546 do not show an electronic density in the 2J5P structure, this implies a low stability or high movement
547 even at cryogenic temperatures. The electron density is shown in blue, while the structure of the ARD
548 determined by X-ray diffraction is fitted to the density and show in ribbon representation. (d) Beta-
549 factor representation in putty cartoon of the crystallographic structure of the ARD in solution (PDBID:
550 2PNN), code color shows red regions have poor density (assumed higher movement) and blue regions
551 have a good density (lower movement).

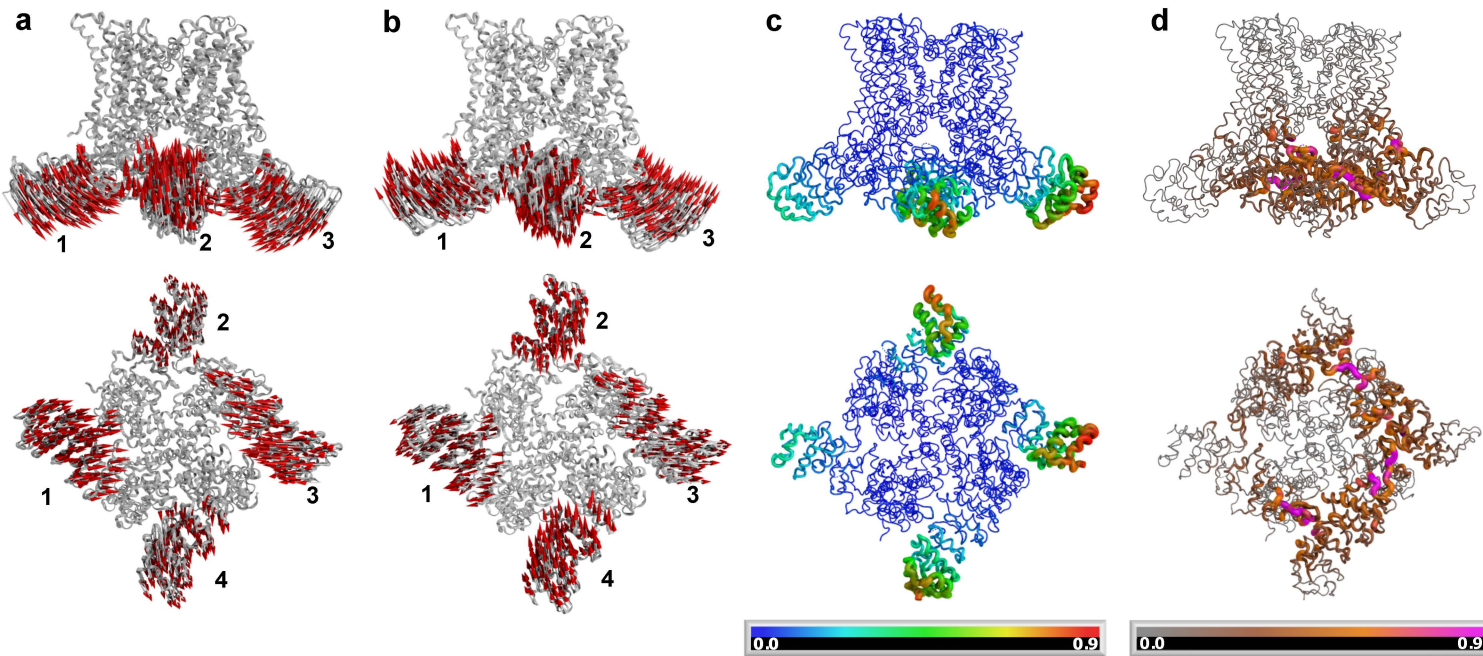
552

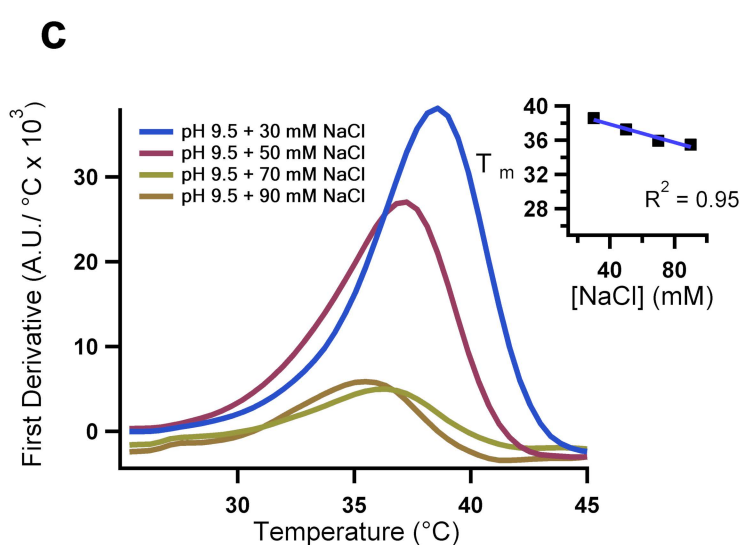
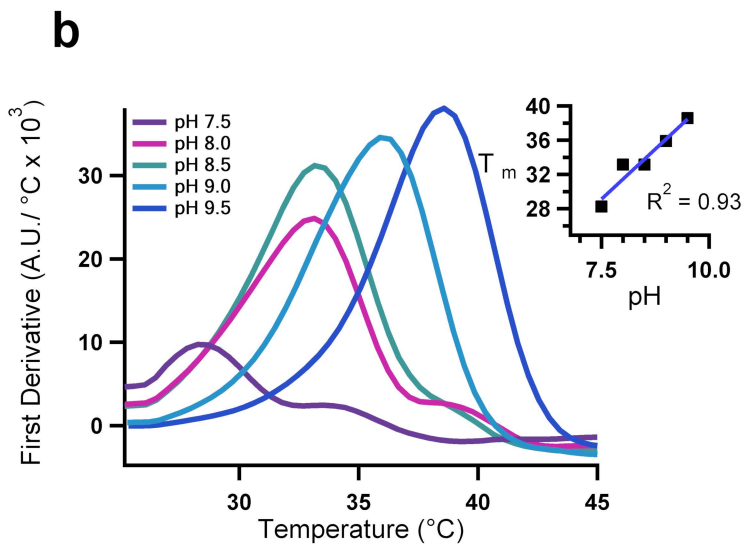
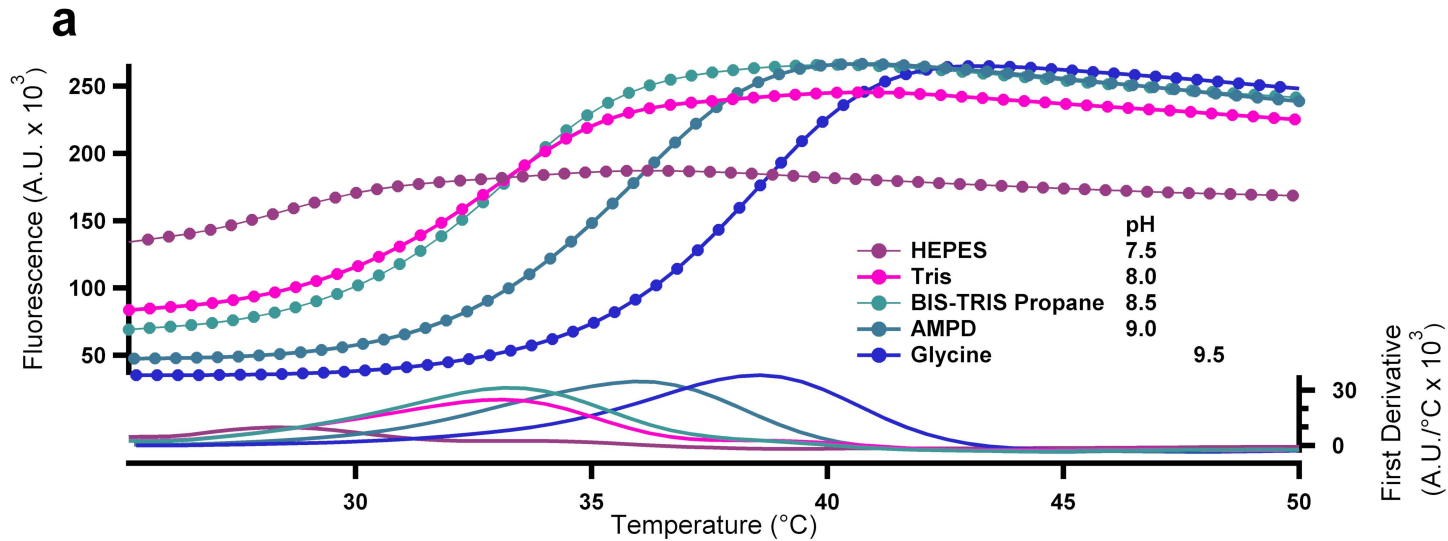
553 **Supplemental Figure 2.** Composite alignment of closed and open structures. (a) Root mean square
554 deviation of CB structure vs. closed structure of TRPV1 (3J5R/3J5P), the color code represents low to
555 high RMSD by the blue to red gradient plotted in Pymol. The gray areas are not aligned by the algorithm.
556 The values are represented over the CB structure; higher variations are seen in the cytosolic regions and
557 the ARD presents higher movement in ANK1 and ANK2. (b) Flexible alignment of DkTx and RTX bound
558 structure vs. closed structure (3J5Q/3J5P). The color code is as in (a). The RMSD is represented over the
559 DkTx+TRX -bound structure. Higher values are seen in ANK 1 and ANK2 and the inner region of the TRP-
560 box. (c) Alignment of the 2APB-bound structure of TRPV3 vs. closed structure of TRPV3 (6DVY/6DVW)
561 represented as in (a). The main changes are similar to CB vs. closed alignment in TRPV1 (a). The color
562 bars indicate the RMSD value scale.

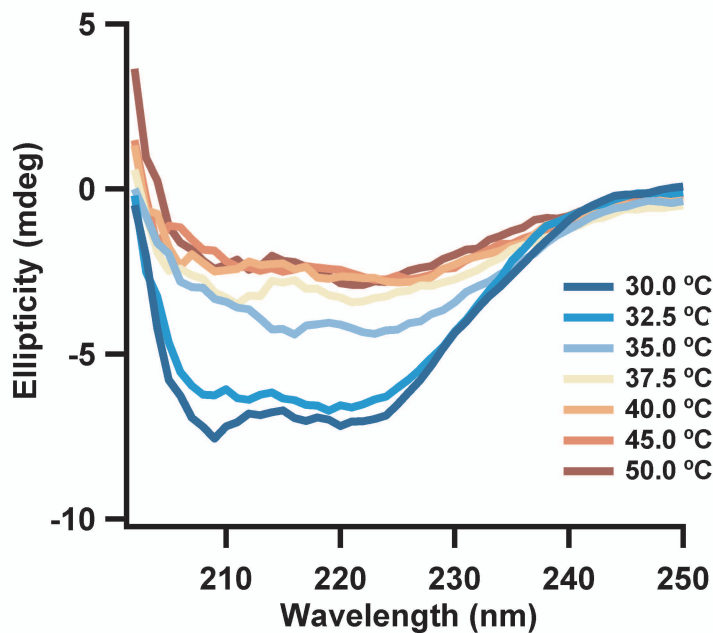
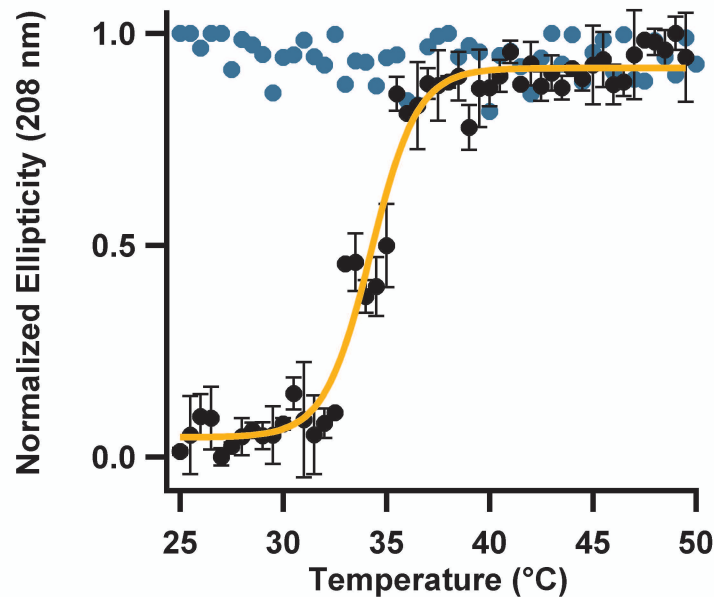
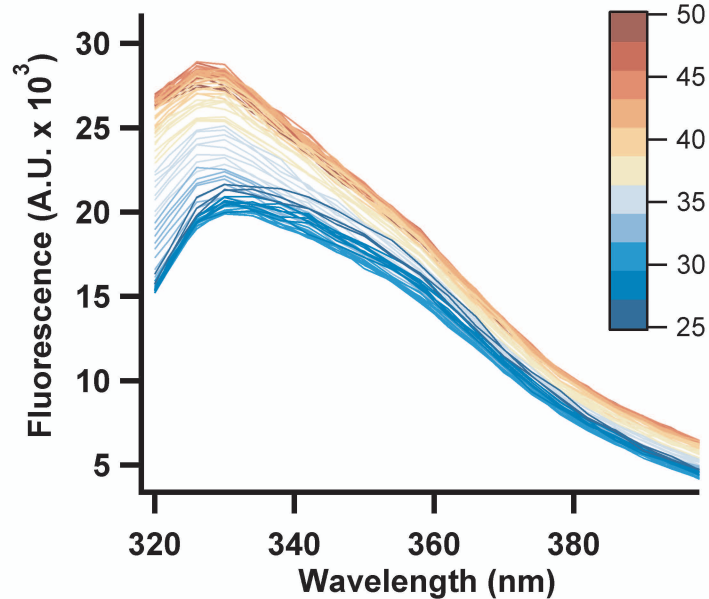
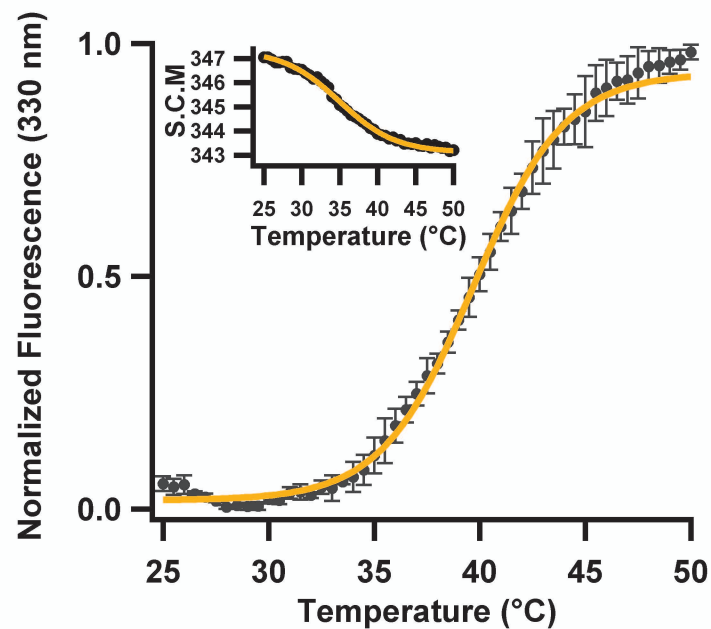
563

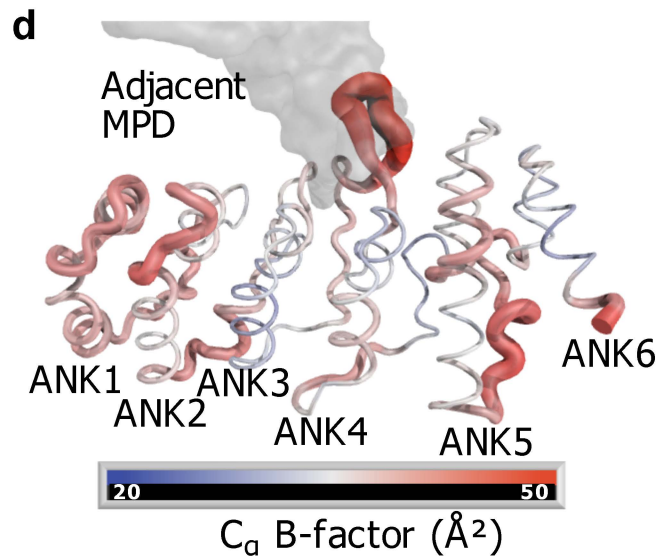
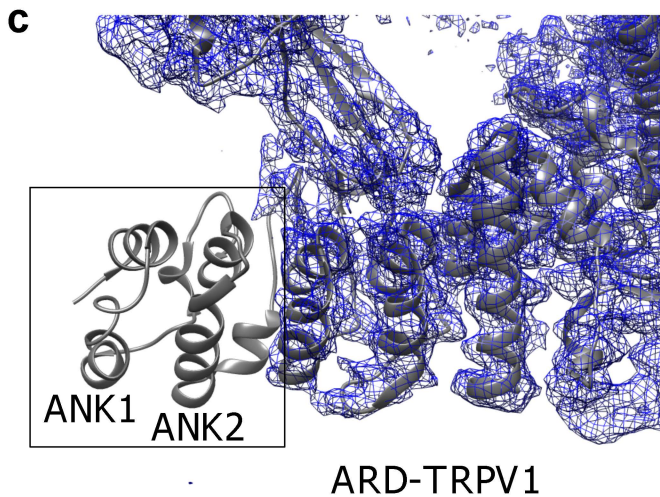
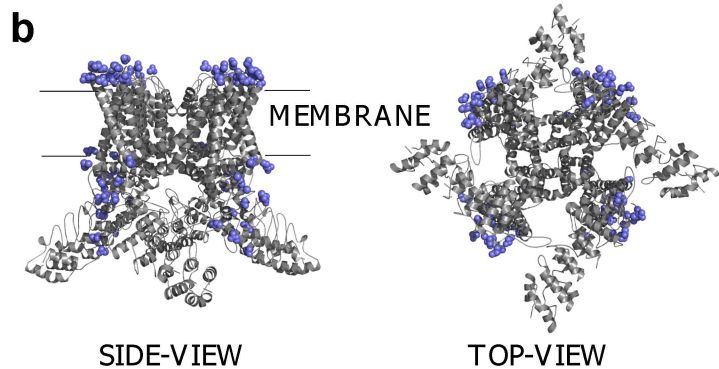
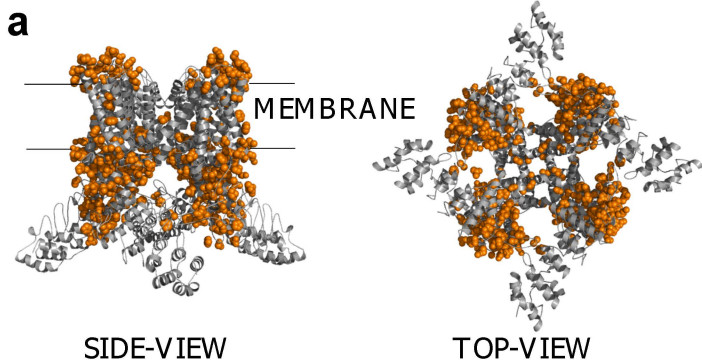
564 **Supplemental Figure 3.** SEC-MALS of isolated ankyrin repeat domain. Chromatogram obtained in 20 mM
565 glycine, pH 9.5, 200 mM NaCl, 25 °C. The peak (arrows) corresponds to a population with MW = 32.4 kDa
566 and $R_g = 3.1$ nm. Colors correspond to light scattering (red), refractive index (blue) and molar mass
567 (black).

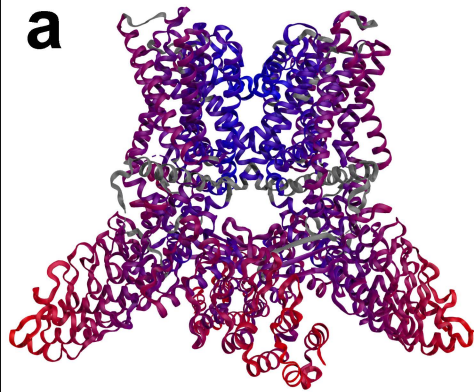
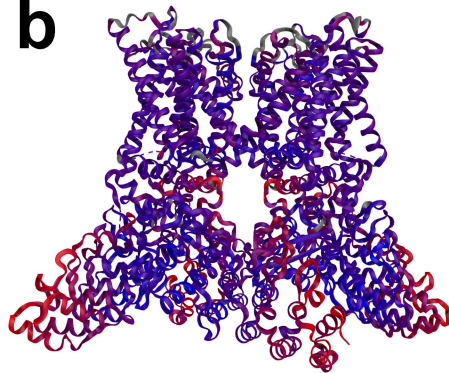
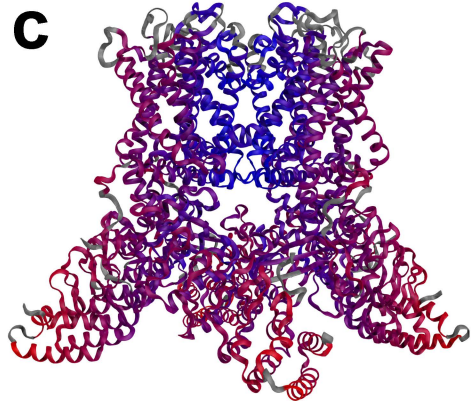
a**b****c**







a**b****c****d**



a**b****c**

5.06  100.50
RMSD (Å)

0.82  9.84
RMSD (Å)

6.53  99.81
RMSD (Å)

SEC-MALS of Ankyrin Repeat Domain (ARD)

